Inorganic Chemistry

Article

pubs.acs.org/IC

Magnetic and Thermodynamic Properties of Nanosized Zn Ferrite with Normal Spinal Structure Synthesized Using a Facile Method

Yunong Zhang,[†] Quan Shi,*[,‡] Jacob Schliesser,[§] Brian F. Woodfield,[§] and Zhaodong Nan*[,†]

[†]College of Chemistry and Chemical Engineering, Yang Zhou University, 225002 Yangzhou, People's Republic of China

[‡]Thermochemistry Laboratory, Dalian Institute of Chemical Physics, Chinese Academy of Sciences, Dalian, Liaoning 116023, People's Republic of China

[§]Department of Chemistry and Biochemistry, Brigham Young University, Provo, Utah 84602, United States

ABSTRACT: Normal spinel zinc ferrite ($ZnFe_2O_4$) nanoparticles (NPs) with zero net magnetization were synthesized by a facile coprecipitation method in which two kinds of organic alkali, namely, 1-amino-2-propanol (MIPA) and bis(2-hydroxypropyl)-amine (DIPA), were used. The diameters of the $ZnFe_2O_4$ NPs were determined to be about 7 and 9 nm for samples prepared with MIPA and DIPA, respectively, and the normal spinel structure was confirmed by the magnetic property measurement at room temperature and the temperature dependence of the direct current magnetization. These results are different from those reported in the literature, where $ZnFe_2O_4$ NPs show a nonzero net magnetization. The heat capacity of the $ZnFe_2O_4$ NPs synthesized using DIPA was measured using a physical property measurement system in the temperature range from 2 to 300 K, and the thermodynamic functions were calculated based on the curve fitting of the experimental heat capacity data. The heat capacity of the $ZnFe_2O_4$ NPs was compared with that of a nanosized $(Zn_{0.795}Fe_{0.205})[Zn_{0.205}Fe_{1.795}]O_4$ material studied in the literature, indicating that the Debye temperature of the present sample is more comparable with that of the bulk $ZnFe_2O_4$ reported by Westrum et al.

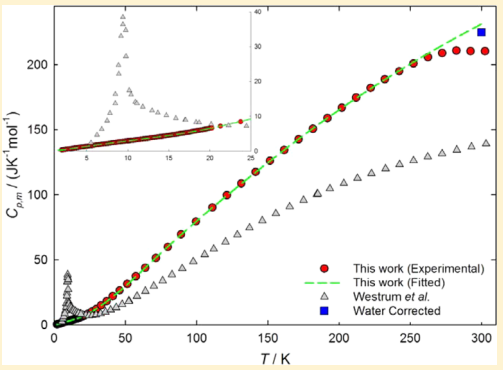

1. INTRODUCTION

Zinc ferrite ($ZnFe_2O_4$) is an important member of the ferrite family and exhibits a variety of remarkable physical properties, such as high specific surface areas, low resistivity, and fascinating electrical and magnetic properties.[1,2] This compound has also received considerable attention over the last two decades because of its technological applications in ferrofluid, medical imaging, drug targeting, magnetic data storage, and catalysis.[3−5] Bulk $ZnFe_2O_4$ belongs to a normal spinel structure with Zn^{2+} ions residing in the tetrahedral sites (A sites) and Fe^{3+} ions in the octahedral sites (B sites),[6] and this structure can be generally presented using a formula of $(Zn^{2+})[Fe^{3+}{}_2]O^{2-}{}_4$, where the parentheses and square brackets denote A and B sites, respectively. In the molecular structure of $ZnFe_2O_4$, the Fe^{3+} ions located in B sites tend to have two sublattices with an opposite magnetic moment, which results in a zero net magnetic property at ambient temperature and an antiferromagnetic property below about 10 K; however, in $ZnFe_2O_4$ nanoparticles (NPs), both the Zn^{2+} and Fe^{3+} ions can be found in either A or B sites and form a mixed spinel structure of $(Zn^{2+}{}_{1-x}Fe^{3+}{}_x)[Zn^{2+}{}_xFe^{3+}{}_{2-x}]O^{2-}{}_4$, where x is the inversion degree,[7] and consequently the opposite magnetic moment in the two Fe^{3+} sublattices are changed and can yield a nonzero net magnetic moment.

Obviously, the inversion degree of $ZnFe_2O_4$ NPs mentioned above may play a crucial role in understanding the molecular structure and the corresponding magnetic property of the compound; therefore, a number of studies have focused on techniques to synthesize $ZnFe_2O_4$ NPs with different inversion degrees.[4,8−10] For instance, Thomas et al.[11] reported a sol−gel method and performed a magnetization study using neutron diffraction and Mössbauer spectroscopy showing that the cationic distribution in the $ZnFe_2O_4$ NPs could vary from that of the bulk form which contributes to the magnetization behavior; furthermore, both A and B site magnetic moments values may vary with temperature which correlates with variations in bond lengths and lattice constants. Bullita et al. synthesized nanocomposite samples supporting $ZnFe_2O_4$ NPs on a silica aerogel porous matrix and found that the superparamagnetic transition temperature is mainly determined by the inversion degree.[12] Moreover, Gomes et al. designed and prepared $ZnFe_2O_4$ NPs using a soft chemistry method to elaborate magnetic nanocolloids and showed that an understanding of the internal atomic arrangement in the nanoparticles at each step of chemical synthesis is essential to account for their magnetic properties.[13]

However, it is still a challenge to synthesize $ZnFe_2O_4$ NPs with a zero net magnetization as observed in the bulk material, and to the best of our knowledge, the synthesis of such NPs has never been reported. In this study, the $ZnFe_2O_4$ NPs with a normal spinal structure have been prepared by a coprecipitation

Received: June 28, 2014
Published: September 5, 2014

   dx.doi.org/10.1021/ic501487c | *Inorg. Chem.* 2014, 53, 10463−10470

method involving two kinds of organic bases as precipitants, namely, 1-amino-2-propanol (MIPA) and bis(2-hydroxypropyl)-amine (DIPA), and the sample characterization was performed using a number of techniques, such as X-ray diffraction (XRD), Fourier transform infrared spectroscopy (FT-IR), inductively coupled plasma-optical emission spectroscopy (ICP-OES), X-ray photoelectron spectroscopy (XPS), transmission electron microscopy (TEM), and thermogravimetric analysis (TGA). Additionally, the magnetic and thermodynamic properties of the as-synthesized $ZnFe_2O_4$ NPs have been studied using a superconducting quantum interference device (SQUID) and a physical property measurement system (PPMS).

2. EXPERIMENTAL SECTION

Synthesis of Normal $ZnFe_2O_4$ Nanoparticles. All reagents were of analytical grade and used as received without further treatment, and all solutions were prepared with twice-distilled water. Starting solutions were prepared by dissolving $ZnCl_2$ in a mixed solution of 1 mL of 37 wt % HCl and 4 mL water to make a 10 mM solution, and $FeCl_3{\cdot}6H_2O$ was dissolved in 40 mL water to make a 20 mM solution. These two solutions were mixed at 50 °C then quickly added to 200 mL of 3.0 M MIPA or DIPA solutions (pH = 11−12) at 100 °C with vigorous mechanical stirring. A red precipitate was immediately generated in the mixture. The mixture was stirred for about 2 h at 100 °C and then cooled to room temperature. The precipitate was obtained from a centrifugal separation process, and the final product was washed with water and ethanol several times before being dried in a vacuum oven at 50 °C for 12 h. The samples are labeled as $ZnFe_2O_4$ (M) and $ZnFe_2O_4$ (D) corresponding to the $ZnFe_2O_4$ NPs prepared with MIPA and DIPA, respectively.

Characterization. TEM and high-resolution transmission electron microscopy (HRTEM) patterns were obtained using a JEOL-2010 TEM with an accelerating voltage of 200 kV. XRD patterns were recorded at room temperature using a Bruker D8 Advanced XRD diffractometer with Cu Kα radiation (λ = 1.542 Å). FT-IR spectroscopy was performed in transmission mode using a Nicolet Aexus 470. The magnetization was measured at room temperature using an MPMS-XL-7 superconducting quantum interference device (MPMS, USA). The temperature dependence of the direct current (DC) magnetization, $\mathbf{M}(T)$, was measured under an external magnetic field of 1000 Oe between 2 and 400 K using a superconducting quantum interference device (SQUID) magnetometer (MPMS, USA). Elemental analysis was performed by using a Perkin Elmer ICP-OES Optima 7300 DV in which 0.0220 g of the sample was dissolved in 1 mL of 37 wt % HCl and then diluted with water to a total volume of 1000 mL. XPS spectra were recorded on a Thermo VG ESCALAB250 X-ray photoelectron spectrometer at a pressure of about 2×10^{-9} Pa using the Al Kα X-ray as the excitation source. The binding energy (BE) from the spectra were calibrated against the C 1s peak located at BE = 284.8 eV. To quantify the amount of adsorbed water, TGA was carried out in corundum crucibles with a heating rate of 10 K/min to 1073 K under flowing nitrogen using a Netzsch 409 TGA system.

Determination of Heat Capacity. The heat capacities of the $ZnFe_2O_4$(M) were measured using a Quantum Design PPMS in zero magnetic field with logarithmic spacing from 2 to 100 K in 10 K temperature intervals from 100 to 300 K and smaller intervals (from 0.1 to 0.2 K) in the temperature region of many possible thermal anomalies. The accuracy of the heat capacity measurements has been established by performing measurements on a high-purity copper pellet and was found to be ±2% from 2 to 20 K and ±0.6% from 20 to 300 K.[14] The powdered sample was measured using a technique that, for both conducting and nonconducting powdered samples, can achieve an accuracy of ±2% below 10 K and ±1% from 10 to 300 K. The details of the sample preparation and the heat capacity experimental procedure can be found in our previous work.[15] The mass of the sample used in this measurement is 15.46 mg.

3. RESULTS AND DISCUSSION

XRD, FT-IR, ICP-OES, XPS, TEM, and TGA. XRD patterns of the as-synthesized samples given in Figure 1 show good

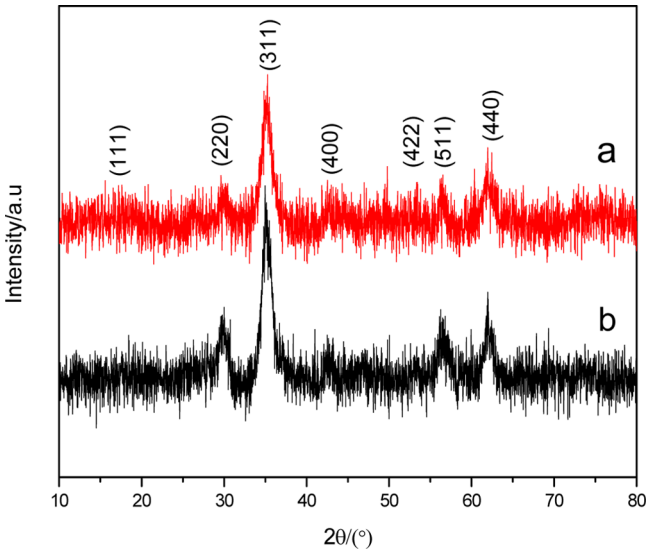

Figure 1. XRD diffraction patterns of ZnFe2O4 prepared under different organic alkali, (a) MIPA, (b) DIPA.

correspondence with the standard patterns of the cubic structure spinel-phase $ZnFe_2O_4$ ($Fd\bar{3}m$(227), JCPDS file No. 82−1049), where the diffraction peaks at 2θ values of 30, 35, 43, 53, 57, and 62° can be attributed to the reflections of (220), (311), (400), (422), (333), and (440) planes, respectively. In previous reports,[5,16] $ZnFe_2O_4$ was synthesized with $Zn(NO_3)_2$, $Fe(NO_3)_3$, and NaOH or ammonia, as reactants. MFe_2O_4 (M = Fe, Co, Mn) was prepared by the aqueous coprecipitation method under alkaline conditions using MIPA, DIPA substituted NaOH or ammonia as the base.[17]

The Bragg equation was used to calculate the lattice constant for the prominent peak (311), and the average crystallite size of the samples was determined from the full width half maxima (fwhm) of the (311) reflection in the XRD patterns using the Debye−Scherrer formula. The lattice constant and the average crystallite size were determined to be 0.8357 and 7.2 nm for the $ZnFe_2O_4$(M), and 0.8438 and 9.0 nm for the $ZnFe_2O_4$(D), respectively.

The presence of the spinel structure for the $ZnFe_2O_4$ samples is further confirmed by FTIR spectroscopy as shown in Figure 2, in which "a" represents the $ZnFe_2O_4$(M) and "b" represents the $ZnFe_2O_4$(D). Figure 2 shows two characteristic absorption peaks in each spectrum at about 554 and 415 cm^{-1} (curve a) and 553 and 414 cm^{-1} (curve b), which can be assigned to the stretching vibrations of the Zn−O bonds in tetrahedral positions and the Fe−O bonds in octahedral positions,[18−20] respectively.

The molar ratio of Zn to Fe contained in the samples was determined by ICP-OES to be 1.0/2.0, which demonstrates the formation of stoichiometric $ZnFe_2O_4$. To reveal the valence states and the chemical composition of the $ZnFe_2O_4$ NPs, the Zn 2p, Fe 2p, and O 1s core level spectra were determined by X-ray photoelectron spectroscopy (XPS). Figures 3a and 4a show the survey spectra of $ZnFe_2O_4$(M) and $ZnFe_2O_4$(D), respectively. As shown in Figures 3b and 4b, a single sharp peak located at 1021.8 eV accounts for the Zn $2p_{3/2}$ level at A site in

dx.doi.org/10.1021/ic501487c | Inorg. Chem. 2014, 53, 10463−10470

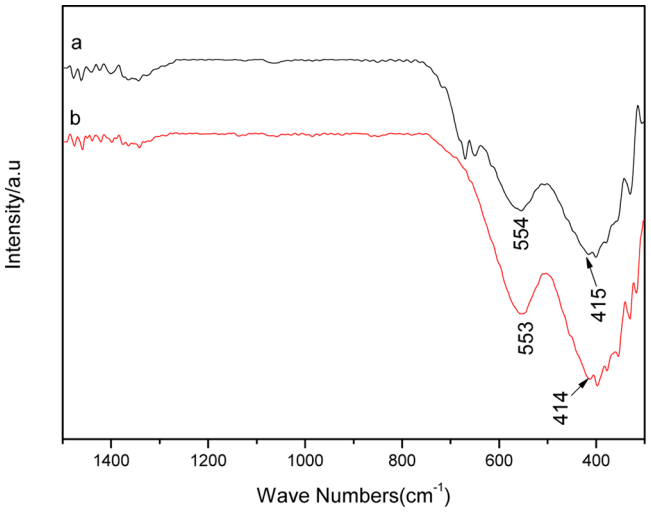

Figure 2. FTIR spectroscopy of ZnFe2O4 prepared under different organic alkali, (a) MIPA, (b) DIPA.

$ZnFe_2O_4$[21] indicating that $ZnFe_2O_4$(M) and $ZnFe_2O_4$(D) both have the normal spinel structure. In Figures 3c and 4c, the Fe 2p core levels are split into Fe $2p_{1/2}$ and Fe $2p_{3/2}$ with binding energies of 711.0(1) and 725.1(2) eV, respectively, and two shakeup satellites exist at 718.8 and 733.4(1) eV. The profile shapes and peak positions are indicative of the presence of Fe^{3+} cations as expected for the $ZnFe_2O_4$.[22,23] The XPS spectrum of the O 1s region was also detected, as shown in Figures 3d and 4d. The O 1s peak is asymmetric with two distinguishable peaks at about 529.5 and 530.8 eV, which are likely due to the lattice oxygen atoms and surface absorbed species (such as metal−OH or water molecules).[24−26]

TEM images seen in Figure 5 show that the average particle diameters are about 7 and 9 nm for the $ZnFe_2O_4$(M) and the $ZnFe_2O_4$(D), respectively, which agree well with those obtained by XRD. The main reason leading to the different particle size is the base used in the synthesis.[17] Interference fringes (see insets of 5A and 5B) show that the distances between two adjacent planes are about 0.26 nm, which corresponds to the (311) planes of the spinel ferrite. The TGA results in Figure 6 show that at about 500 °C, where all water has been desorbed, $ZnFe_2O_4$(M) and $ZnFe_2O_4$(D) have mass losses of 18.39% and 12.74%, respectively.

Magnetic Property. The magnetic properties of the as-synthesized samples were investigated at room temperature in magnetic fields from −20 to 20 kOe, and the results are shown in Figure 7. The magnetization sharply increases with increasing field strength but even at 20 kOe does not reach a saturation state. This suggests that ferromagnetic and paramagnetic interactions coexist through strong paramagnetic intercluster interactions mixed with ferromagnetic interactions inside the clusters.[27,28] The ferromagnetic property tends to become saturated with increasing applied field, while the paramagnetic property increases linearly.[29] The magnetization **M** shows a linear dependence on magnetic field strength **H** as the following,

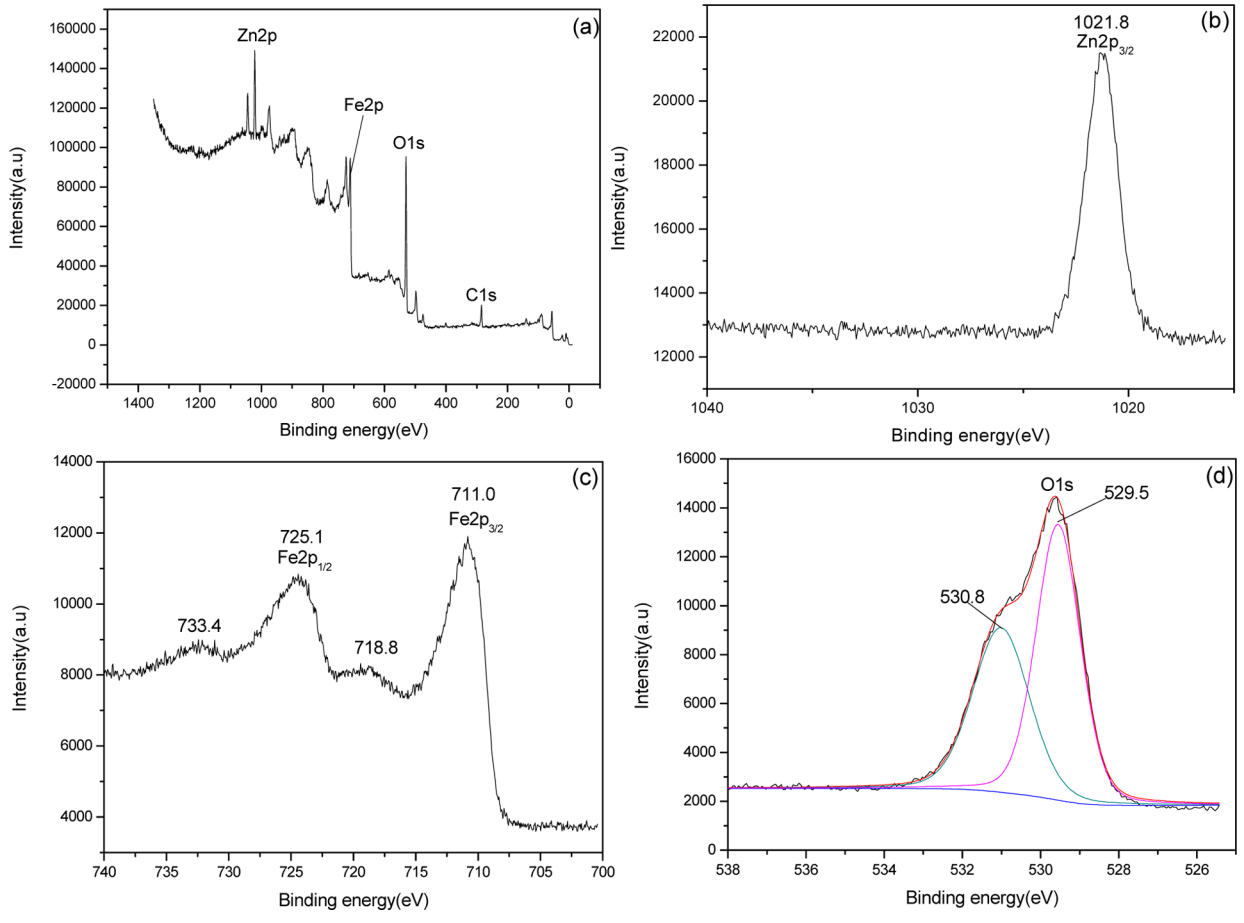

Figure 3. XPS spectra of the ZnFe2O4 prepared with MIPA: the survey spectra of the sample (a), Zn 2p (b), Fe 2p (c), and O 1s (d).

dx.doi.org/10.1021/ic501487c | Inorg. Chem. 2014, 53, 10463−10470

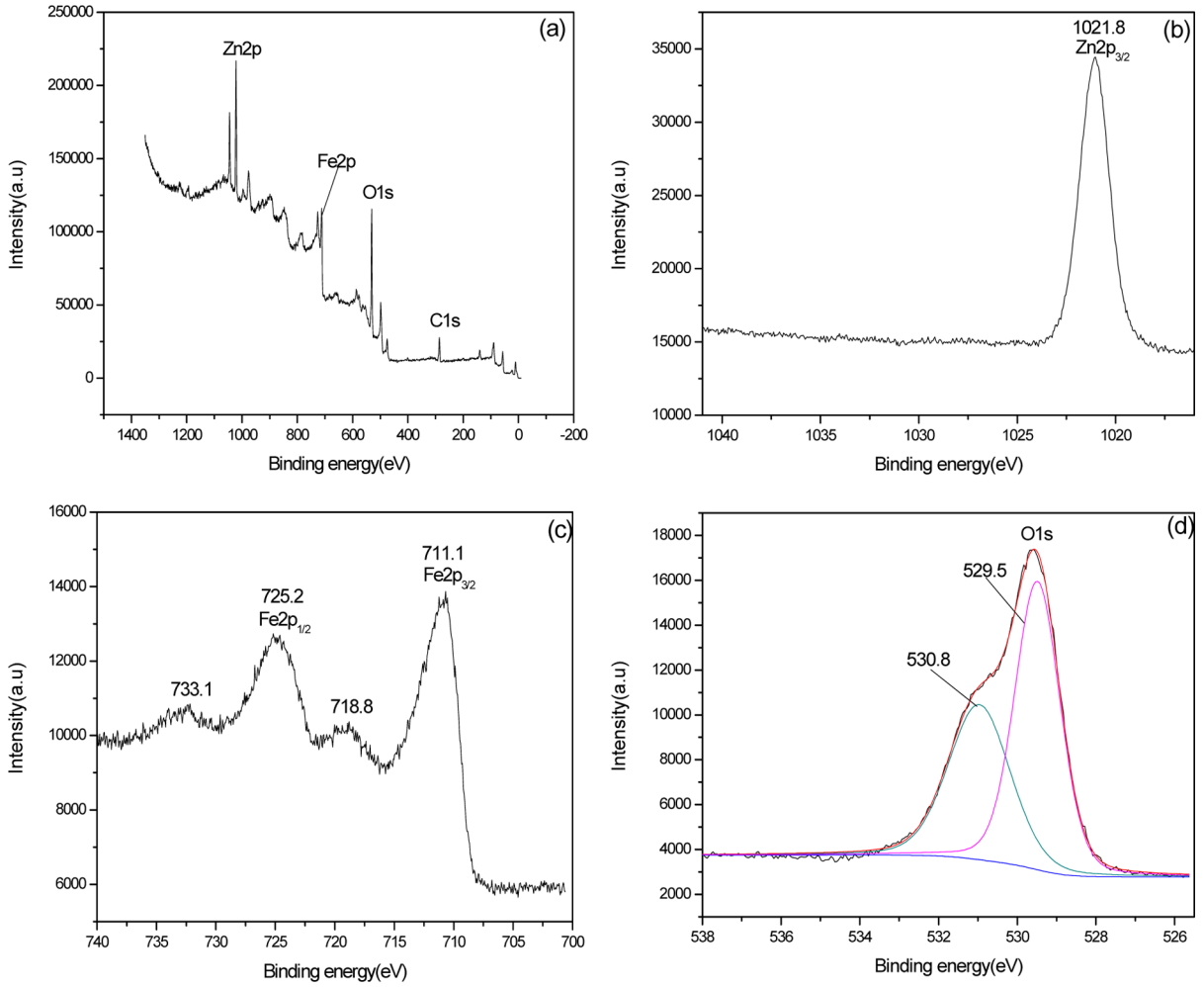

Figure 4. XPS spectra of the ZnFe2O4 prepared with DIPA: the survey spectra of the sample (a), Zn 2p (b), Fe 2p (c), and O 1s (d).

$$\mathbf{M} = \mathbf{M}_0 + \chi\mathbf{H} \quad (1)$$

where $\mathbf{M}_0$ (emu/g) is the extrapolated magnetization at zero field and χ (emu·g^{-1}·Oe^{1-}) is the high field susceptibility.

For $ZnFe_2O_4$(M)

$$\mathbf{M} = 2.589 \times 10^{-4}\mathrm{H} - 1.330 \times 10^{-4}$$
$$R^2 = 0.9982 \quad (2)$$

For $ZnFe_2O_4$(D)

$$\mathbf{M} = 2.133 \times 10^{-4}\mathrm{H} - 6.496 \times 10^{-5}$$
$$R^2 = 0.9998 \quad (3)$$

where R^2 is the correlation coefficient.

The hysteresis curves of $ZnFe_2O_4$ NPs previously investigated exhibit the typical "S"-like shape,[4] which can be divided into curvature and linearity. In the present study, the hysteresis curve is solely linear which is attributed to the paramagnetic phase of the sample[30] suggesting that $ZnFe_2O_4$ NPs with a normal bulk spinel structure (which is paramagnetic) were successfully synthesized with MIPA and DIPA.

In order to study the effect of temperature on the magnetization of the sample, the temperature dependence of zero-field-cooled magnetization $\mathbf{M}_{ZFC}(T)$ and field-cooled magnetization $\mathbf{M}_{FC}(T)$ were determined at an external magnetic field of 1000 Oe for the $ZnFe_2O_4$(M), and the results are shown in Figure 8. It can be seen that both $\mathbf{M}_{ZFC}(T)$ and $\mathbf{M}_{FC}(T)$ monotonically increase as temperature decreases and diverge after passing through the spin freezing temperature, T_f, which for the ZFC magnetization curve lies at 16 K. Such a FC−ZFC difference at low temperatures is often seen in spin-glass or spin-glass-like materials.[31−33] Bulk $ZnFe_2O_4$ is paramagnetic down to the Neel temperature of 10 K, where it becomes antiferromagnetic. When the magnetization of such a system under a suitable magnetic field is plotted against the temperature, it gives a spin freezing temperature near the Neel temperature.[34] Such a behavior is caused by the disordered distribution of Zn^{2+} and Fe^{3+} ions in the spinel structure and can be explained in terms of superparamagnetism with intercluster interactions.[35] When the T_f is at lower temperatures, it can reduce the strength of strong superexchange interactions between Fe^{3+} ions occupied at A and B sites, and the distribution of Zn^{2+} and Fe^{3+} ions are more similar to the normal spinel structure.[36] The results are in agreement with the magnetic property obtained in Figure 7, which further confirms that the $ZnFe_2O_4$(M) in this study has the normal spinel structure.

Heat Capacity. The heat capacity of the $ZnFe_2O_4$(M) sample was measured in the temperature range from 2 to 300 K using a physical property measurement system (PPMS). Nanoparticles absorb water when exposed to air, so to obtain accurate heat capacity data of the current sample, the amount of

dx.doi.org/10.1021/ic501487c | Inorg. Chem. 2014, 53, 10463−10470

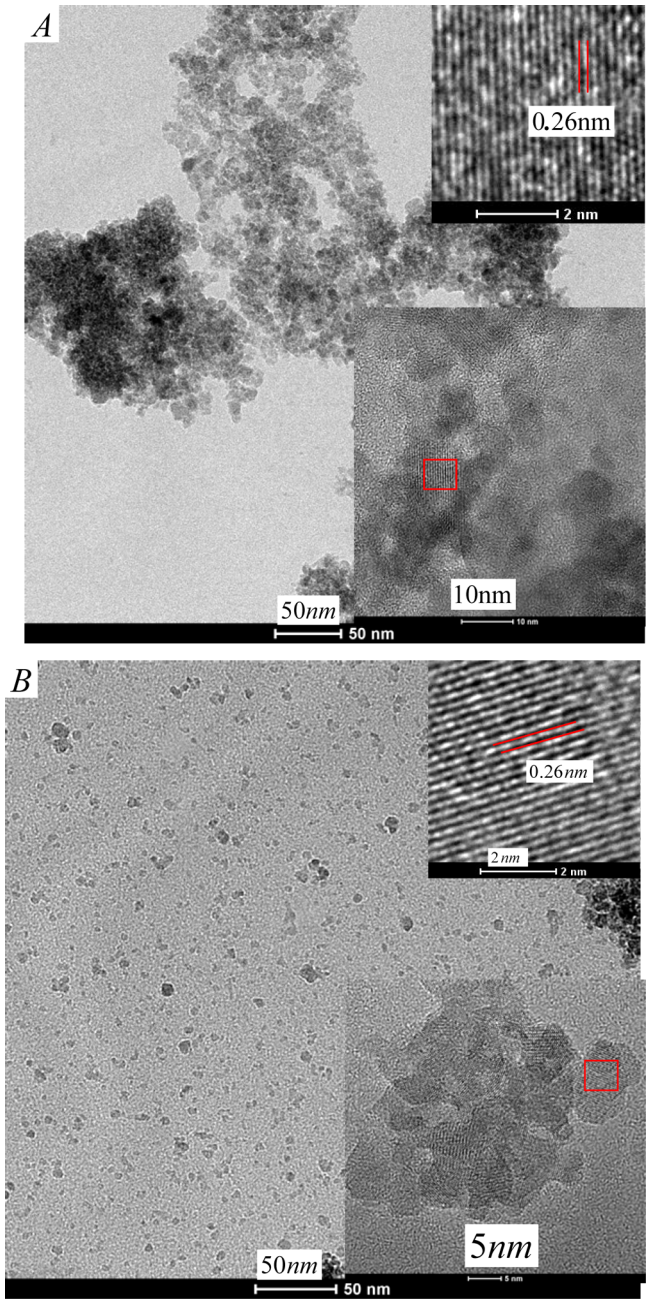

Figure 5. TEM images of the samples prepared with MIPA (A) and DIPA (B). (insets) HRTEM images.

water on the sample must be known. Assuming all the mass loss in the TGA measurement (Figure 6) is from water desorption, then the chemical formula of the sample can be corrected to $ZnFe_2O_4 \cdot 1.955\ H_2O$ with a molecular weight of 276.27 g/mol. This corrected value was used to calculate the heat capacity data, which are shown in Figure 9.

It can be seen in Figure 9 that there are no obvious phase transitions or other thermal anomalies in the heat capacity curve below 250 K; however, above 250 K there is a noticeable broad peak or decrease in the heat capacity slope. In reality, this does not stem from any intrinsic characteristics of the sample but is likely due to the water absorbed on the sample starts to come off above about 250 K in the high vacuum during the measurement. To confirm that this anomaly is related to water loss, 99.73 mg of sample were placed under vacuum in room

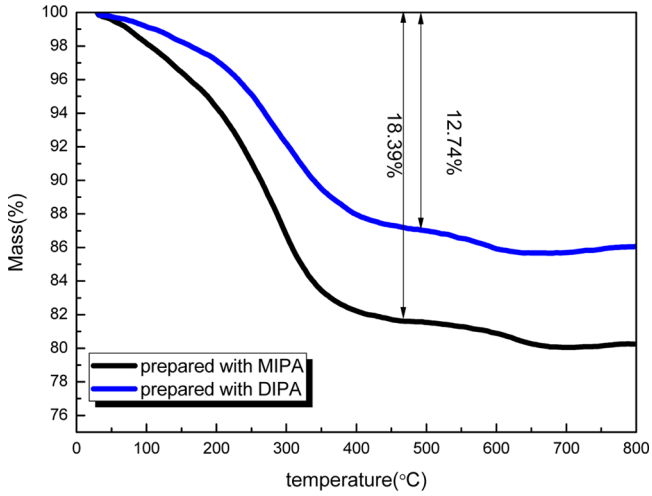

Figure 6. TGA curves for the ZnFe2O4 NPs.

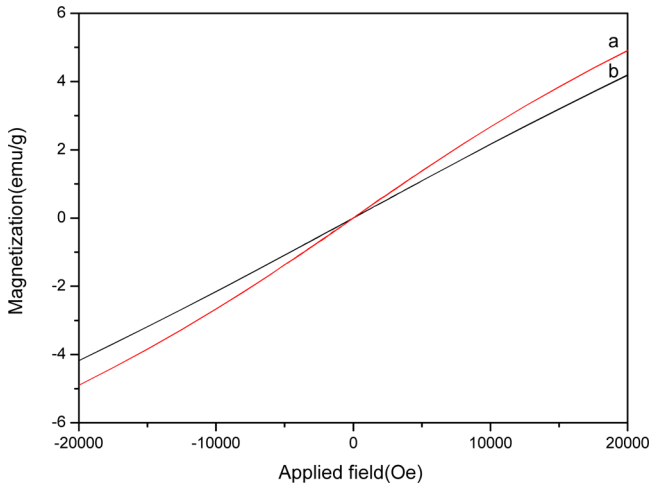

Figure 7. Magnetization curve of ZnFe2O4 prepared with MIPA (a) and DIPA (b).

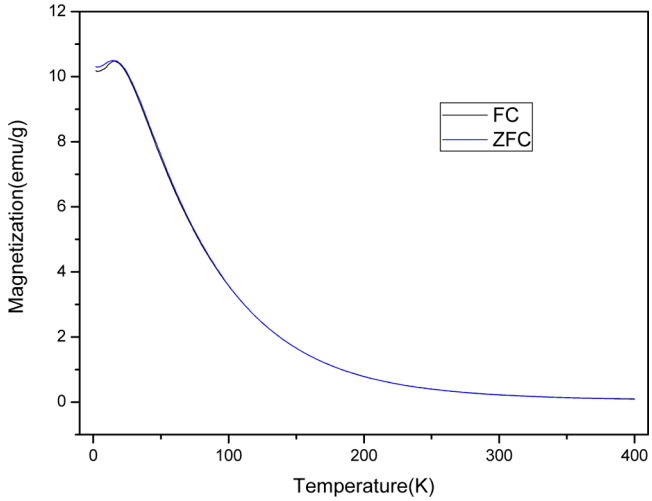

Figure 8. FC and ZFC magnetizations at H=1000 Oe for the ZnFe2O4(M).

temperature. After several hours the sample had lost 2.33 mg of mass which we attribute to water desorption. We note that because the heat capacity measurement started at 1.9 K, no

dx.doi.org/10.1021/ic501487c | Inorg. Chem. 2014, 53, 10463−10470

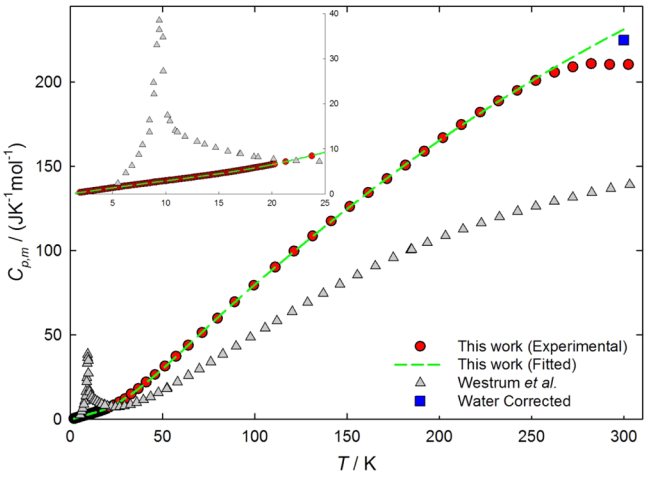

Figure 9. Molar heat capacities of the ZnFe2O4(M) compared with the bulk ZnFe2O4 by Westrum et al.[43] (inset) The data below 25 K.

water was lost before 250 K, and all data up to about 250 K represent the heat capacity of $ZnFe_2O_4 \cdot 1.955H_2O$. Assuming that the sample used in the heat capacity measurement lost 2.33% of its mass between 250 to 300 K, the final data point at T = 300 K corresponds to the heat capacity of $ZnFe_2O_4 \cdot 1.596H_2O$. To be able to compare this data point with those of the sample before water was lost, we assume, as a rough estimate, that the heat capacity of the water difference is equal to the heat capacity of hexagonal ice. Adding this heat capacity to that of the data point at T = 300 K yields a heat capacity value that is comparable to the extrapolation from the Debye–Einstein fit (see the square data in Figure 9) demonstrating that this anomaly is likely related to water loss under vacuum.

To alleviate this effect on the thermodynamic calculation, we fitted the experimental data in the temperature range from 40 to 250 K using a combination of Debye and Einstein functions and extrapolate the data through the water desorption region, which is shown using a dashed line in the figure.[37] The Debye–Einstein function used in the fitting is

$$C_{p,m} = n_D D(\theta_D) + n_E E(\theta_E) + A_1 T^1 + A_2 T^2 \quad (4)$$

where $D(\theta_D)$ and $E(\theta_E)$ are Debye and Einstein functions, respectively; n_D, n_E, A_1, and A_2 are adjustable parameters; θ_D and θ_E are the Debye and Einstein temperatures, respectively; the sum of n_D and n_E should be approximately the number of atoms in the molecule; and the T and T^2 terms provide an estimate for the difference between C_p and C_v.[38,39] The fitting parameters are listed in Table 1.

In the low-temperature region (T < 15 K), the heat capacity of a substance is generally interpreted as a sum of lattice, electronic, and magnetic contributions, which may provide important information about the physical properties of a material.[40−42] These contributions can be extracted from the total heat capacity by fitting the data to theoretical models at low temperatures. The heat capacity of the sample below 5 K was fitted to the following equation.

$$C_{p,m} = \gamma T + B_3 T^3 + B_5 T^5 + B_{asw} T^3 \quad (5)$$

where the linear term represents the contribution from defects and/or oxygen vacancies; the odd powers in temperature represents the lattice; and the B_{asw} term represents the antiferromagnetic behavior. Because both the lattice and

Table 1. Parameters for Fits of the Heat Capacity (in J·K^{-1}·mol^{-1}) of the $ZnFe_2O_4$(M)

parameter	temperature range	coefficients
	$0 \le T/K \le 3.13$	
γ		1.2575×10^{-01}
B_{asw}		1.4748×10^{-02}
B_3		2.4428×10^{-04}
B_5		-4.4903×10^{-04}
	RMS% = 0.25	
	$3.13 \le T/K \le 40.50$	
A_0		-2.2301×10^{-01}
A_1		2.4021×10^{-01}
A_2		3.0705×10^{-02}
A_3		-4.3402×10^{-03}
A_4		2.6774×10^{-04}
A_5		-7.6410×10^{-06}
A_6		1.0435×10^{-07}
A_7		-5.5248×10^{-10}
	RMS% = 0.54	
	$40.50 \le T/K \le 305$	
n_D		3.305
θ_D		381.92
n_E		3.602
θ_E		799.56
A_1		3.3939×10^{-01}
A_2		2.2678×10^{-05}
	RMS% = 0.84	

antiferromagnetic heat capacity exhibit a T^3 dependence, it is difficult to separate them from each other in the data fitting. In order to evaluate the sample's antiferromagnetic behavior, the B_3 term was calculated using the Debye temperature obtained in the Debye–Einstein fitting above, and the B_{asw} term was obtained by fitting the data to eq 5 with this fixed B_3 term. The B_{asw} term is determined to be 14.75 mJ·K^{-4}·mol^{-1}, which is comparable to values reported in the heat capacity study of some iron phosphates.[43]

The heat capacity data of the $ZnFe_2O_4$(M) measured in this work were compared with the bulk data reported by Westrum et al.,[44] which are also shown in Figure 9. It can be seen that the heat capacity of $ZnFe_2O_4$(M) is higher than that of the bulk, which is in agreement with previous reports that the heat capacity of nanomaterials can be significantly larger than that of their parent bulk materials.[45−51] This behavior has been mostly attributed to the surface water absorbed on the nanomaterials.[45,37] Moreover, the present $ZnFe_2O_4$ does not exhibit a distinct magnetic transition around 10 K, suggesting that, due to the small particle size, either the transition is likely spread out over a large temperature interval with little enthalpy or an insulating phase with different thermal conductivities appears.[42]

It is worth noting that Ho et al. also measured the heat capacity of $ZnFe_2O_4$ NPs in the temperature range from 1 to 40 K by a thermal relaxation technique;[52] however, their $(Zn_{1-x}Fe_x)[Zn_xFe_{2-x}]O_4$ (x = 0.205) sample synthesized by an aerogel process does not have a normal spinel structure like the bulk material. The heat capacity from Ho et al. is relatively larger than that of the present measurement, and their Debye temperature of 225 K is much smaller than the value of 381.92 K obtained in this work. The Debye temperature of bulk $ZnFe_2O_4$ obtained by Westrum is 425 K which is much more

dx.doi.org/10.1021/ic501487c | Inorg. Chem. 2014, 53, 10463−10470

Table 2. Smoothed Heat Capacities, Gibbs Free Energies, Enthalpies, and Entropies for Nano $ZnFe_2O_4$(M)

T	C_p°	$\Delta_o^T G^\circ$	$\Delta_o^T H^\circ$	$\Delta_o^T S^\circ$	T	C_p°	$\Delta_o^T G^\circ$	$\Delta_o^T H^\circ$	$\Delta_o^T S^\circ$
K	J·mol^{-1}·K^{-1}	J·mol^{-1}	J·mol^{-1}	J·mol^{-1}·K^{-1}	K	J·mol^{-1}·K^{-1}	J·mol^{-1}	J·mol^{-1}	J·mol^{-1}·K^{-1}
0	0	0	0	0	70	50.20	−918.34	1367.53	32.66
1	0.140	−0.0641	0.0665	0.131	75	55.32	−1090.67	1631.36	36.29
2	0.357	−0.271	0.307	0.289	80	60.38	−1281.44	1920.65	40.03
3	0.673	−0.656	0.815	0.490	85	65.36	−1491.06	2235.03	43.84
4	1.01	−1.26	1.66	0.731	90	70.26	−1719.91	2574.11	47.71
5	1.35	−2.12	2.84	0.993	95	75.08	−1968.27	2937.50	51.64
6	1.68	−3.25	4.35	1.27	100	79.84	−2236.38	3324.83	55.61
7	2.00	−4.66	6.19	1.55	110	89.17	−2832.64	4170.06	63.66
8	2.31	−6.36	8.35	1.84	120	98.31	−3509.94	5107.59	71.81
9	2.62	−8.34	10.82	2.13	130	107.28	−4269.14	6135.66	80.04
10	2.92	−10.62	13.59	2.42	140	116.10	−5110.84	7252.70	88.31
11	3.22	−13.18	16.66	2.71	150	124.77	−6035.47	8457.20	96.62
12	3.52	−16.04	20.03	3.01	160	133.27	−7043.26	9747.54	104.94
13	3.83	−19.20	23.71	3.30	170	141.58	−8134.33	11 121.97	113.27
14	4.15	−22.64	27.70	3.60	180	149.70	−9308.68	12 578.58	121.60
15	4.49	−26.39	32.02	3.89	190	157.62	−10 566.20	14 115.36	129.90
16	4.84	−30.43	36.68	4.19	200	165.32	−11 906.66	15 730.20	138.18
17	5.22	−34.78	41.71	4.50	210	172.80	−13 329.77	17 420.96	146.43
18	5.62	−39.43	47.12	4.81	220	180.07	−14 835.16	19 185.48	154.64
19	6.04	−44.40	52.95	5.12	230	187.13	−16 422.40	21 021.62	162.80
20	6.50	−49.68	59.22	5.45	240	193.98	−18 090.99	22 927.31	170.91
25	9.23	−81.14	98.24	7.18	250	200.64	−19 840.41	24 900.54	178.96
30	12.62	−121.85	152.62	9.15	260	207.10	−21 670.08	26 939.40	186.96
35	16.45	−173.06	225.15	11.38	270	213.40	−23 579.40	29 042.04	194.89
40	20.62	−236.01	317.67	13.84	273.15	215.34	−24 197.23	29 717.30	197.38
45	25.10	−311.86	432.04	16.53	280	219.52	−25 567.75	31 206.74	202.77
50	29.82	−401.65	569.21	19.42	290	225.48	−27 634.50	33 431.88	210.57
55	34.77	−506.35	730.60	22.49	298.15	230.24	−29 376.44	35 289.00	216.89
60	39.87	−626.84	917.17	25.73	300	231.30	−29 779.01	35 715.92	218.32
65	45.04	−763.93	1129.43	29.13					

comparable with our results providing further evidence that the $ZnFe_2O_4$ NPs synthesized in this work form a normal spinel structure.

To present the smooth heat capacity in the entire experimental temperature region, the data between 5 and 40 K were fitted to an orthogonal polynomial function, and the fitting parameters as well as those obtained from eq 4 and 5 are listed in Table 1. All the fitted data are plotted in Figure 9 using a dashed line. On the basis of the data fitting, the molar thermodynamic functions have been calculated at selected temperatures from 0 to 300 K, and the calculated results are listed in Table 2. The standard molar entropy has been determined to be (216.89 ± 2.2) J·K^{-1}·mol^{-1} at 298.15 K.

4. CONCLUSIONS

Zinc ferrite nanoparticles were successfully synthesized using a facile coprecipitation method using two kinds of precipitants MIPA and DIPA as precipitants. The sample characterization from the FTIR, ICP-OES, XPS, TEM, and TGA indicated that the as-synthesized nanoparticles have a normal spinel structure similar to bulk $ZnFe_2O_4$, which has never been reported before in the literature. The magnetization was measured using the MPMS and SQUID. This confirmed that this bulk structure is also found in the nanoparticles. The thermodynamic properties of the $ZnFe_2O_4$(M) studied using a PPMS show that the Debye temperature of our sample is more comparable with the bulk result than that of the $ZnFe_2O_4$ nanoparticle with a mixed spinel structure that has been reported in the literature. The thermodynamic functions were calculated based on fitting the experimental heat capacities. The standard molar entropy of $ZnFe_2O_4$·1.596H_2O was determined to be (216.89 ± 2.2) J·K^{-1}·mol^{-1} at 298.15 K.

AUTHOR INFORMATION

Corresponding Authors

*E-mail: zdnan@yzu.edu.cn. Tel: +86-514-87959896. Fax: +86-514-87959896. (Z.N.)

*E-mail: shiquan@dicp.ac.cn. Tel: +86-411-84379213. (Q.S.)

Notes

The authors declare no competing financial interest.

ACKNOWLEDGMENTS

The authors gratefully acknowledge the financial support from the National Nature Science Foundation of China (21273196) and the Priority Academic Program Development of Jiangsu Higher Education Institutions.

REFERENCES

(1) Wang, Y. P.; Li, L. C. *React. Funct. Polym.* **2008**, *68*, 1587−1593.

(2) Li, L. C.; Liu, H. *J. Colloid Interface Sci.* **2008**, *321*, 265−271.

(3) Haetge, J.; Suchomski, C.; Brezesinski, T. *Inorg. Chem.* **2010**, *49*, 11619−11626.

(4) Yao, C.; Zeng, Q.; Goya, G. F.; Torres, T.; Liu, J.; Wu, H. *J. Phys. Chem. C* **2007**, *111*, 12274−12278.

(5) Anantharaman, M. R.; Jagatheesan, S.; Malini, K. A.; Sindhu, S.; Narayanasamy, A.; Chinnasamy, C. N.; Jacobs, J. P.; Reijne, S.; Seshan,

K.; Smits, R. H. H.; Brongersma, H. H. *J. Magn. Magn. Mater.* **1998**, *189*, 83−88.
(6) Jiang, J. Z.; Wynn, P. *Nanostruct. Mater.* **1999**, *12*, 737−740.
(7) Bullita, S.; Casu, A.; Casula, M. F.; Concas, G.; Congiu, F.; Corrias, A.; Falqui, A.; Loche, D.; Marras, C. *Phys. Chem. Chem. Phys.* **2014**, *16*, 4843−4852.
(8) Blanco-Gutierrez, V.; Torralvo-Fernandez, M. J.; Saez-Puche, R. *J. Phys. Chem. C* **2010**, *114*, 1789−1795.
(9) Blanco-Gutierrez, V.; Climent-Pascual, E.; Torralvo-Fernandez, M. J.; Saez-Puche, R.; Fernandez-Diaz, M. T. *J. Solid State Chem.* **2011**, *184*, 1608−1613.
(10) Alves, C. R.; Aquino, R.; Depeyrot, J.; Cotta, T. A.; Sousa, M. H.; Tourinho, F. A.; Rechenberg, H. R.; Goya, G. F. *J. Appl. Phys.* **2006**, *99*, 08M905.
(11) Thomas, J. J.; Shinde, A. B.; Krishna, P. S. R.; Kalarikkal, N. *Mater. Res. Bull.* **2013**, *48*, 1506−1511.
(12) Bullita, S.; Casu, A.; Casula, M. F.; Concas, G.; Congiu, F.; Corrias, A.; Falqui, A.; Loche, D.; Marras, C. *Phys. Chem. Chem. Phys.* **2014**, *16*, 4843−4852.
(13) Gomes, J. A.; Azevedo, G. M.; Depeyrot, J.; Mestnik-Filho, J.; Paula, F. L. O.; Tourinho, F. A.; Perzynski, R. *J. Phys. Chem. C* **2012**, *116*, 24281−24291.
(14) Shi, Q.; Snow, C. L.; Boerio-Goates, J.; Woodfield, B. F. *J. Chem. Thermodyn.* **2010**, *42*, 1107−1115.
(15) Shi, Q.; Boerio-Goates, J.; Woodfield, B. F. *J. Chem. Thermodyn.* **2011**, *43*, 1263−1269.
(16) Chen, Z. P.; Fang, W. Q.; Zhang, B.; Yang, H. G. *J. Alloys Comp.* **2013**, *550*, 348−352.
(17) Pereira, C.; Pereira, A. M.; Fernandes, C.; Rocha, M.; Mendes, R.; Fernández-García, M. P.; Guedes, A.; Tavares, P. B.; Grenèche, J. M.; Araújo, J. P.; Freire, C. *Chem. Mater.* **2012**, *24*, 1496−1504.
(18) Li, Y. B.; Yi, R.; Yan, A. G.; Deng, L. W.; Zhou, K. C.; Liu, X. H. *Solid. State. Sci.* **2009**, *11*, 1319−1324.
(19) Hankare, P. P.; Patil, R. P.; Jadhav, A. V.; Pandav, R. S.; Garadkar, K. M.; Sasikala, R.; Tripathi, A. K. *J. Alloys. Compd.* **2011**, *509*, 2160−2163.
(20) Lopez, F. A.; Lopez-Delgado, A.; Martin-de-Vidales, J. L.; Vila, E. *J. Alloys. Compd.* **1998**, *265*, 291−296.
(21) Druska, P.; Steinike, U.; Sepelak, V. *J. Solid. State. Chem.* **1999**, *146*, 13−21.
(22) Wang, M.; Ai, Z.; Zang, L. *J. Phys. Chem. C* **2008**, *112*, 13163−13170.
(23) Wen, M.; Li, Q.; Li, Y. *J. Electron Spectrosc. Relat. Phenom.* **2006**, *153*, 65−70.
(24) Sharma, Y.; Sharma, N.; Rao, G. V. S.; Chowdari, B. V. R. *Electrochim. Acta* **2008**, *53*, 2380−2385.
(25) Marco, J. F.; Gancedo, J. R.; Gracia, M.; Gautier, J. L.; Rios, E. I. *J. Solid. State. Chem.* **2000**, *153*, 74−81.
(26) Tavares, A. C.; Da Silva Pereira, M. I.; Mendonca, M. H.; Nunes, M. R.; Costa, F. M.; Sa, C. M. *J. Electroanal. Chem.* **1998**, *449*, 91−100.
(27) Bhowmik, R. N.; Ranganathan, R. *J. Magn. Magn. Mater.* **2002**, *248*, 101−111.
(28) Fiorani, D.; Vitiocoli, S.; Dorman, J. L.; Tholence, J. L.; Murani, A. P. *Phys. Rev. B* **1984**, *30*, 2776−2786.
(29) Köseoğlu, Y.; Baykal, A.; Toprak, M. S.; Gözüak, F.; Basaran, A. C.; Aktas, B. *J. Alloys. Compd.* **2008**, *462*, 209−213.
(30) Li, F.; Wang, H.; Wang, L.; Wang, J. *J. Magn. Magn. Mater.* **2007**, *309*, 295−299.
(31) Huang, C. Y. *J. Magn. Magn. Mater.* **1985**, *51*, 1−74.
(32) Soubeyroux, J. L.; Fiorani, D.; Agostinelli, E. *J. Magn. Magn. Mater.* **1986**, *83*, 54−57.
(33) Ishikawa, T.; Ebisu, S.; Nagata, S. *Condens. Matter.* **2010**, *405*, 1881−1889.
(34) Upadhyay, C.; Verma, H. C.; Sathe, V.; Pimpale, A. V. *J. Magn. Magn. Mater.* **2007**, *312*, 271−279.
(35) Nakashima, S.; Fujita, K.; Tanaka, K.; Hirao, K. *J. Phys.: Condens. Matter* **2005**, *17*, 137−149.
(36) Nakashima, S.; Fujitaa, K.; Tanaka, K.; Hirao, K.; Yamamoto, T.; Tanaka, I. *J. Magn. Magn. Mater.* **2007**, *310*, 2543−2545.
(37) Shi, Q.; Boerio-goates, J.; Woodfield, K.; Rytting, M.; Pulsipher, K.; Spencer, E. C.; Ross, N. L.; Navrotsky, A.; Woodfield, B. F. *J. Phys. Chem. C* **2012**, *116*, 3910−3917.
(38) Shi, Q.; Park, T.-J.; Schliesser, J.; Navrotsky, A.; Woodfield, B. F. *J. Chem. Thermodyn.* **2014**, *72*, 77−84.
(39) Woodfield, B. F.; Boerio-Goates, J.; Shapiro, J. L.; Putnam, R. L.; Navrotsky, A. *J. Chem. Thermodyn.* **1999**, *31*, 245−253.
(40) Gopal, E. S. R. *Specific Heats at Low Temperatures;* International Cryogenics Monograph Series, Plenum Press: New York,1966.
(41) Snow, C. L.; Shi, Q.; Boerio-Goates, J.; Woodfield, B. F. *J. Chem. Thermodyn.* **2011**, *42*, 1136−1141.
(42) Snow, C. L.; Shi, Q.; Boerio-Goates, J.; Woodfield, B. F. *J. Phys. Chem. C* **2010**, *114*, 21100−21108.
(43) Shi, Q.; Zhang, L.; Schlesinger, M. E.; Boerio-Goates, J.; Woodfield, B. F. *J. Chem. Thermodyn.* **2013**, *62*, 86−91.
(44) Westrum, E. F.; Grimes, D. M. *J. Phys. Chem. Solids* **1957**, *3*, 44−49.
(45) Boerio-Goates, J.; Li, G.; Li, L.; Walker, T. F.; Parry, T.; Woodfield, B. F. *Nano Lett.* **2006**, *6*, 750−754.
(46) Volokitin, Y.; Sinzig, J.; de Jongh, L. J.; Schmid, G.; Vargaftik, M. N.; Moiseev, I. I. *Nature* **1996**, *384*, 621−623.
(47) Chen, Y. Y.; Yao, Y. D.; Hsaio, S. S.; Jen, S. U.; Lin, B. T.; Lin, H. M.; Tung, C. Y. *Phys. Rev. B* **1995**, *52*, 9364−9369.
(48) Sun, N. X.; Lu, K. *Phys. Rev. B* **1996**, *54*, 6058−6061.
(49) Terwilliger, C. D.; Chiang, Y. M. *J. Am. Ceram. Soc.* **1995**, *78*, 2045−2055.
(50) Zhang, H.; Banfield, J. F. *Nanostruct. Mater.* **1998**, *10*, 185−194.
(51) Wolf, D.; Wang, J.; Gleiter, H. *Phys. Rev. Lett.* **1995**, *74*, 4686−4689.
(52) Ho, J. C.; Hamdeh, H. H.; Chen, Y. Y.; Lin, S. H.; Yao, Y. D.; Willey, R. J.; Oliver, S. A. *Phys. Rev. B* **1995**, *52*, 10122−10126.